engineering proceedings

MDPI

Proceeding Paper

Numerical and Experimental Analysis of the Structural Behavior of an EPP Component †

Carlo Sabbatini [1,*], Gianluca Chiappini [2], Veronica Ilari [1], Giacomo Zandri [1] and Marco Sasso [1]

[1] Department of Industrial Engineering and Mathematical Sciences, Università Politecnica delle Marche, 60131 Ancona, Italy; s1114472@studenti.univpm.it (V.I.); g.zandri@staff.univpm.it (G.Z.); m.sasso@staff.univpm.it (M.S.)
[2] Department of Industrial Engineering, Università degli studi eCampus, 22060 Novedrate, Italy; g.chiappini@staff.univpm.it
* Correspondence: c.sabbatini@pm.univpm.it
† Presented at the 53rd Conference of the Italian Scientific Society of Mechanical Engineering Design (AIAS 2024), Naples, Italy, 4–7 September 2024.

Abstract: The use of expanded polymeric materials is becoming increasingly widespread in the industrial sector, not only for energy absorption purposes but also for structural applications. The most widely used approach to model the large strain elastic response of polymer foams in a finite element (FE) solution is the use of the Ogden–Hill hyperelastic material model. We performed a uniaxial and simple shear test to calibrate the model's parameters. In this work, a compression test was performed on a component, entirely made of expanded polypropylene, from a commercial machine. The experimental results, measured through 3D image analysis, were then compared with the simulation ones. This study aims to verify whether the Ogden foam model accurately describes the material's behavior when the component has a complex geometry and large dimensions.

Keywords: polymer foams; parameter fitting; Ogden model; digital image correlation

check for updates

Academic Editors: Umberto Galietti, Gabriele Arcidiacono, Enrico Armentani, Davide Castagnetti, Vigilio Fontanari, Aurelio Somà and Nicola Bonora

Published: 27 February 2025

Citation: Sabbatini, C.; Chiappini, G.; Ilari, V.; Zandri, G.; Sasso, M. Numerical and Experimental Analysis of the Structural Behavior of an EPP Component. *Eng. Proc.* **2025**, *85*, 29. https://doi.org/10.3390/engproc2025085029

Copyright: © 2025 by the authors. Licensee MDPI, Basel, Switzerland. This article is an open access article distributed under the terms and conditions of the Creative Commons Attribution (CC BY) license (https://creativecommons.org/licenses/by/4.0/).

1. Introduction

Expanded polypropylene (EPP) is a closed-cell polymeric foam already widely used as energy absorber in sectors such as the automotive industry, personal protective equipment, and other fields [1,2]. These applications are due to its cellular structure, which provides the capability of crushing it up into large deformations with limited loads [3]. The two-phase structure of polypropylene foam, composed of solid polymeric material cells containing gas, typically air at ambient pressure, interconnected to form a complex grid, provides a low density, and good thermal [4] and acoustic insulation properties [5]. Additionally, the low cost of the material, combined with its ability to be molded into complex geometries, makes it appropriate for its use, in the form of expanded polypropylene, in the construction of load-bearing structures. This latter application will be the focus of the subsequent phases of this study.

Under axial loading conditions, the highly nonlinear behavior of the stress–strain curve is related to the different deformation mechanisms of the cells. Specifically, the deformation can involve cell wall bending, elastic buckling, or plastic yielding. In the case of closed-cell foams, like the one we are considering, the mechanical response to compression is characterized by three distinct phases. Figure 1 shows the stress–strain curve, considering positive values for compression, for an expanded polypropylene specimen subjected to a compression test, where the three phases are clearly distinguished.

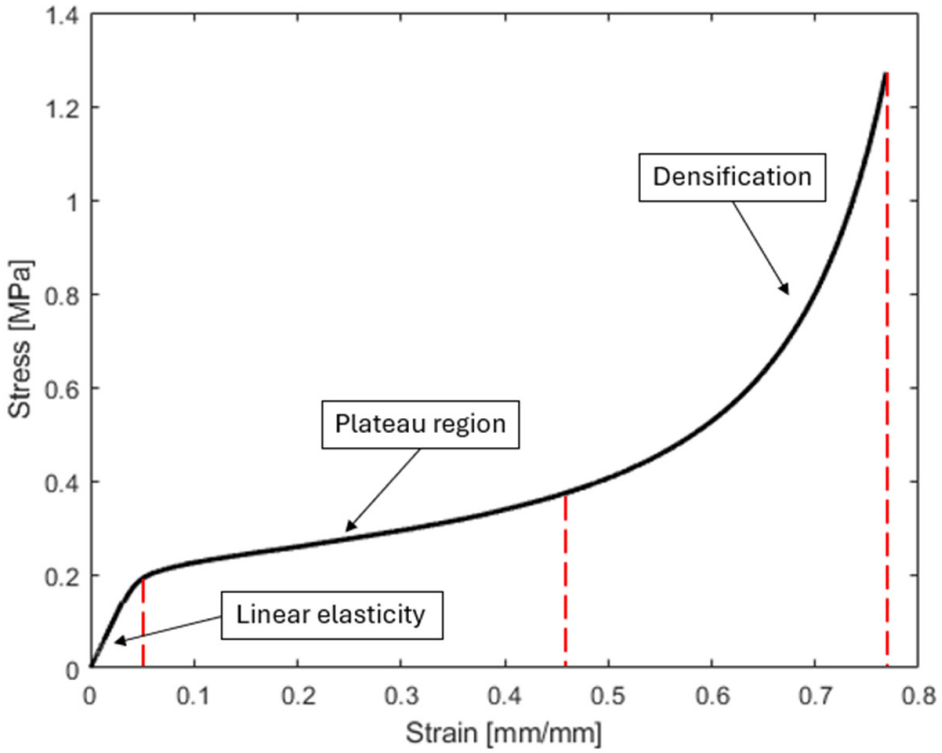


Figure 1. Stress–strain curve for a compression load.

In the first phase, for small strains (below 5%), cell walls bend or distort to accommodate deformation, leading to a linear elastic response in the stress–strain curve. The second phase is characterized by a plateau region, where large plastic or elastic deformations occur, depending on the foam's base material, in response to small stress variations. This plateau region is critical for energy absorption, as it is governed by the elastic buckling of the cell walls. The third phase is called densification, which occurs when the foam cells are fully collapsed upon each other (around 60% engineering strain). In this final phase, the solid material of the cell walls interacts directly with the adjacent cell walls, leading to a rapid increase in stiffness. The densification strain corresponds to the strain in which the cell structure is thoroughly compacted. The foam material, when compressed beyond its densification strain, behaves more like its solid base material than a cellular one. The theoretical densification strain can be defined as the strain which corresponds to the zero-void volume state, and it is equal to the material porosity $(1 - \rho^*/\rho_s)$. However, experimental tests show an increase in stiffness at a strain well below the theoretical value of the densification strain is reached. This can be defined as onset densification strain; in fact, at this deformation, cell walls and edges start to interact which each other. Gibson and Ashby propose an equation that properly predicts the onset densification strain using a correction factor in the porosity density law,

$$\varepsilon_{cd} = \left(1 - 1.4\left(\frac{\rho^*}{\rho_s}\right)\right) \quad (1)$$

where ε_{cd} is the onset densification strain, and $\rho*$ and ρ_s are the foam and its solid base material densities, respectively [6].

To accurately describe the nonlinear behavior of foams, it is necessary to correctly characterize one of the nonlinear hyperelastic material models available in the literature. In this work, the Ogden foam model is used; it is based on the strain energy density function

(W) and is affected by the shape deformation (λ_i) and volume change of the foamed sample (J) [7].

$$W(\lambda_1, \lambda_2, \lambda_3) = \sum_{i=1}^{N} \frac{\mu_i}{\alpha_i} \left(\lambda_1^{\alpha_i} + \lambda_2^{\alpha_i} + \lambda_3^{\alpha_i} - 3 + \frac{1}{\beta_i} \left(J^{-\alpha_i \beta_i} - 1 \right) \right) \quad (2)$$

where λ_k (k = 1, 2, 3) represent the principal stretches, J denotes the volume ratio (determinant of the deformation gradient F), N is the order of the model, and μ_i, α_i and β_i are the hyperelastic material parameters. These parameters are obtained by fitting experimental data from several mechanical tests [8].

In this work, we performed a compression test on a component made entirely of expanded polypropylene, sourced from a commercial product. A large-sized component with a complex geometry was selected to induce a deformation state distinct from that observed during the experimental tests used to calibrate the hyperelastic model. The deformation field was measured using Digital Image Correlation (DIC) technology.

Multiple measure zones were defined to observe the overall component's behavior under force stress. Stereo DIC, involving a pair of cameras for each zone, led to full-field displacement maps. This technique entails the definition of a reference subset with sufficient gray intensity variations picked up from the reference image. Then, by means of a predefined criterion and a certain optimization algorithm, the DIC technique searches the deformed image for the deformed subset, the intensity pattern of which is of maximum similarity with the reference subset [9].

Experimental results were compared with numerical simulations in regions where the displacement was most significant, with the aim of validating the Ogden foam model. The goal of this study is to verify and assess the capability of using this properly calibrated model to simulate structural behavior of expanded polypropylene for industrial applications.

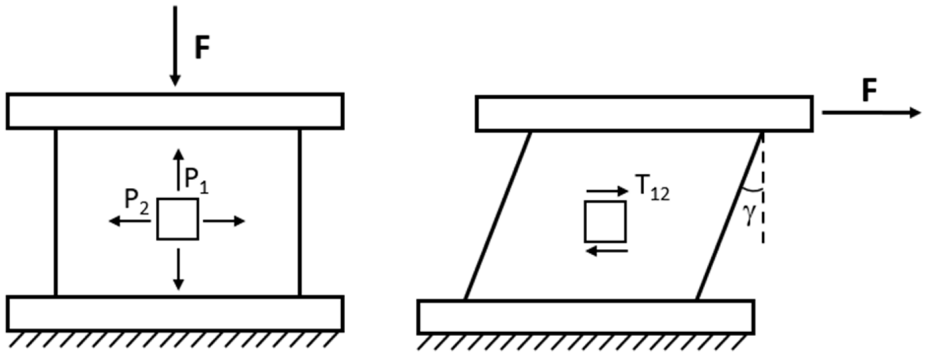
2. Material and Experimental Procedures

In this work, parallelepiped samples of closed-cell expanded polypropylene foam were tested to characterize the constitutive behavior of the material. The EPP foam samples were taken from two different components of the same company product, with a nominal density of 50 kg/m^3.

EPP foam components generally comprise smaller beads, molded into shape. Polypropylene (PP) pellets are pressurized and expanded into foamed beads, typically measuring 2–4 mm in diameter. These beads are then further expanded in a mold where higher temperatures allow the PP to melt, sintering the beads into the final shape of the components.

2.1. Uniaxial Compression and Tensile Tests

Uniaxial compressions and tensile tests were performed in a static material tensile machine (ZwickRoell 50,) with a calibrated 5 kN load cell. For compression tests, foam samples had a nominal 25 mm × 25 mm square section, the length of samples was 20 mm and specimens were placed between two parallel plates, as shown in Figure 2a. For tensile tests, the prismatic samples (15 × 15 × 25 mm) were bonded to aluminum supports, which were gripped by the tensile machine. In both cases, the crosshead velocity was imposed in order to always conduct the tests at a 10^{-3} s^{-1} strain rate. From each sample, when necessary, a 5 mm layer was removed to eliminate the skin left on the piece during production by the mold walls.



(**a**) (**b**)

Figure 2. Representation of (**a**) uniaxial compression test, P_1 and P_2 are principal stresses; (**b**) simple shear test, T_{12} is shear stress.

2.2. Simple Shear Tests

A good description of the mechanical behavior of foam materials under complex loading conditions requires different mechanical tests, beyond the commonly used uniaxial test. For this reason, we also performed simple shear tests; briefly, the tests were conducted by bonding a prismatic specimen between two aluminum supports [10]. Once gripped by the testing machine, roughly parallel and opposite movements were applied to the supports moving the machine test's crosshead, in order to generate a shear stress state in the center of the specimen (Figure 2b). This type of test is very simple but can introduce some experimental problems:

- The shear stress distribution is not homogeneous over the sample;
- During the test, the material close to two opposite corners of the sample is subjected to transverse tension, while the material close to the other two corners is subjected to compression.

In order to minimize these issues as much as possible, the specimens were prepared with a length-to-width ratio (L/h) major of 10 to reduce the inhomogeneity in the shear stress state [11]. Additionally, deformations were recorded using Digital Image Correlation in the central area of the specimen to also minimize edge effects.

3. Model Responses for Specific Deformations

As mentioned in the introduction, this work considers the hyperelastic model formulated by Ogden. This model is available in the most commonly used finite element analysis software and is suitable for modeling both the static and time-dependent response of polymer foams. The model is based on the strain energy function, which depends on principal stretches, defined as $\lambda = \frac{L_f}{L_0} = 1 + \varepsilon$.

$$W(\lambda_1, \lambda_2, \lambda_3) = \sum_{i=1}^{N} \frac{\mu_i}{\alpha_i} \left(\lambda_1^{\alpha_i} + \lambda_2^{\alpha_i} + \lambda_3^{\alpha_i} - 3 + \frac{1}{\beta_i} \left(J^{-\alpha_i \beta_i} - 1 \right) \right) \quad (3)$$

where N is the order of the model, J denotes the volume ratio (a determinant of the deformation gradient F), and μ_i, α_i, β_i are model parameters: μ_i has the unit of stress; in fact, it is directly correlated with the initial shear modulus G. On the other hand, α_i and β_i are both dimensionless; in particular, α_i represents the hardening or softening exponent of the model and β_i is related to the effective Poisson's ratio ν.

$$G = \sum_{i=1}^{N} \frac{\mu_i \alpha_i}{2} \quad \nu_i = \frac{\beta_i}{1 + 2\beta_i} \tag{4}$$

3.1. Stress Solution

Starting from a hyperelastic strain energy potential W, the first Piola–Kirchhoff stress tensor **P**, can be obtained as follows:

$$\mathbf{P} = \sum_{k=1}^{3} \frac{\partial W}{\partial \lambda_k} \mathbf{n}_k \otimes \mathbf{N}_k \tag{5}$$

where λ_k are the principal stretches, $\mathbf{N}_k$ and $\mathbf{n}_k$ are the eigenvectors in the reference and the current configuration, respectively, and P_k represents the principal stresses [12]. Substituting the strain energy function expressed according to the Ogden model into the equation just derived, we obtain the relation for the principal nominal stresses of the hyperelastic model:

$$P_k = \frac{1}{\lambda_k} \sum_{i=1}^{N} \mu_i \left(\lambda_k^{\alpha_i} - J^{-\alpha_i \beta_i} \right), \quad k = 1, 2, 3 \tag{6}$$

The stress solutions for the deformation imposed during the experimental test are reported in the following paragraphs.

3.2. Uniaxial Stress

Considering the case of uniaxial deformation, and for simplicity, assuming the stretch along the loading direction is $\lambda_1 = \lambda$, while the stretches in the other directions, i.e., the transverse ones, are $\lambda_2 = \lambda_3 = \lambda_t$, given that the material is isotropic, we can write the deformation gradient F and the volume ratio J as follows:

$$F = \begin{bmatrix} \lambda & 0 & 0 \\ 0 & \lambda_t & 0 \\ 0 & 0 & \lambda_t \end{bmatrix} \qquad J = \det F = \lambda \lambda_t^2 \tag{7}$$

Having measured a Poisson's ratio of approximately zero through DIC during the compression test, we can further simplify the matrix since $\lambda_t = 1$, and thus $J = \lambda$. Taking this into account, we can express the stresses as follows:

$$\begin{gathered} \sigma_1 = P_1 = \frac{1}{\lambda_1} \sum_{i=1}^{N} \mu_i \left(\lambda_1^{\alpha_i} - 1 \right) \\ \sigma_2 = \sigma_3 = P_2 = P_3 = 0 \end{gathered} \tag{8}$$

3.3. Shear Stress

In the case of the shear test, considering direction 1 as the one parallel to the imposed displacement and direction 2 as the normal one, perpendicular to the glued surface of the specimen, the deformation gradient in the case of simple shear can be expressed as follows:

$$F = \begin{bmatrix} 1 & \gamma & 0 \\ 0 & 1 & 0 \\ 0 & 0 & 1 \end{bmatrix} \tag{9}$$

from which the principal stretches, the function of γ, can be obtained considering a plane strain state, i.e., $\lambda_3 = 1$ [13].

$$\lambda_1 = \sqrt{\frac{1}{2}\left(2+\gamma^2+\gamma\sqrt{4+\gamma^2}\right)} = \frac{1}{2}\left(\gamma+\sqrt{\gamma^2+4}\right) \tag{10}$$

$$\lambda_2 = \sqrt{\frac{1}{2}\left(2+\gamma^2-\gamma\sqrt{4+\gamma^2}\right)} = \frac{1}{2}\left(-\gamma+\sqrt{\gamma^2+4}\right) \tag{11}$$

It should be noted that J = 1 implies that $\lambda_2 = 1/\lambda_1$. In accordance with Equation (6), the solution for the principal stress is as follows:

$$\tau = T_{12} = \left(\left(\frac{\gamma}{2}+\frac{1}{2}\sqrt{\gamma^2+4}\right)^{-1}\right)\sum_{i=1}^{N}\mu_i\left(\left(\frac{\gamma}{2}+\frac{1}{2}\sqrt{\gamma^2+4}\right)^{\alpha_i}-1\right) \tag{12}$$

3.4. Parameter Fitting

As can be seen from Equation (2), in the case of the third-order Ogden model (n = 3), nine parameters must be determined. These material parameters need to be chosen so that the model best describes the experimental behavior of the material.

To calibrate the parameters, we simultaneously fit both Equations (8) and (12), using the value of λ_t obtained from DIC experimental measurements [14]. Since during compression we have a stretch approximately equal to 1, it follows that the Poisson's ratio can be assumed to be zero. Thus, the values of the parameters $\beta_i = 0$ can be obtained, recalling the physical meaning that links them to Poisson's ratio according to Equation (4). To simultaneously fit both the uniaxial and shear tests, error functions were defined, in which the error functions for the uniaxial tension and shear were summed up with equal weight. These are defined as follows:

$$\begin{gathered} err_{uniax} = \frac{\left|\sigma_{exp}-\sigma_1\right|}{\sqrt{n}} \quad err_{shear} = \frac{\left|\tau_{exp}-\tau_1\right|}{\sqrt{n}} \\ Err_{tot} = err_{uniax}+err_{shear} \end{gathered} \tag{13}$$

where σ_{exp} and τ_{exp} are, respectively, the experimental uniaxial and shear stress, while n is the number of points at which the deviation was calculated [15].

To minimize the total error function, we used the built-in function "minimize" in Matlab software R2024b. Thise function allowed us to find the set of parameters that would minimize the total error, while simultaneously satisfying the physical constrain of μ_i and α_i:

$$G = \sum_{i=1}^{N}\frac{\mu_i\alpha_i}{2} > 0 \tag{14}$$

Since the initial shear modulus cannot take a negative value, we performed fitting over a reduced strain range, based on the expected structural use. The fitting results are reported in Table 1 and in Figure 3, where we show the model's strain–stress curve, compared with the experimental results.

Table 1. Fitting coefficients of the third-order Ogden hyperfoam model.

μ_1	μ_2	μ_3	α_1	α_2	α_3	β_i
14.94	20.87	74.05	−1.85	0.22	0.42	0

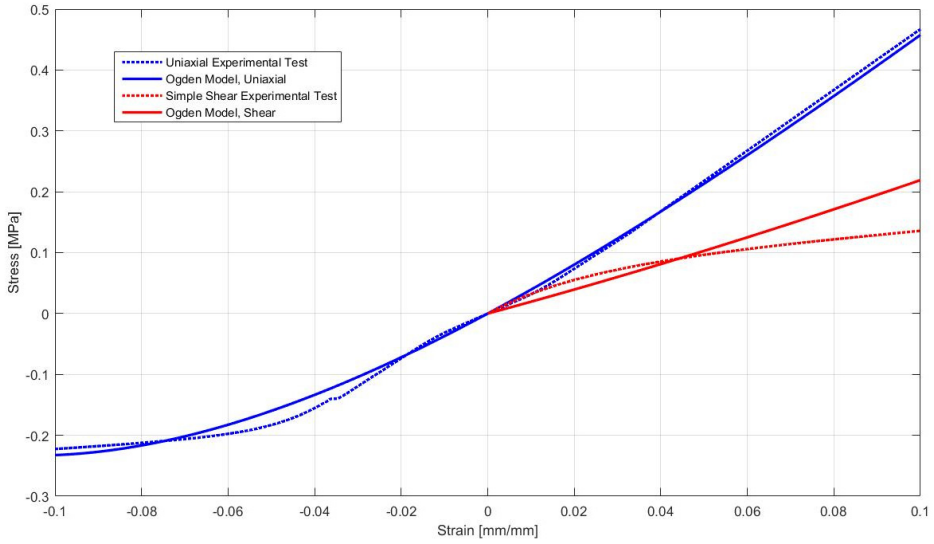


Figure 3. Plot of fitting results.

4. Test on Real Component

We decided to conduct a compression test on a large EPP component with a structural role, part of a more complex assembly, to validate the newly calibrated model. The aim was to create a complex stress and strain state through an actual geometry, differing from those of the experimental tests used to fit the parameters. In fact, one of the main issues of this calibration method is that it ensures accurate correspondence only in describing the mechanical behavior of the stress and strain states on which it was fitted [16].

With this test, we aim to assess the feasibility of using a calibration system that requires only few experimental tests, while still ensuring the ability to simulate even complex structural problems.

4.1. Component Preparation

All additional parts of the component were made of metal or solid polymer, disassembled and removed, resulting in a structure entirely composed of expanded polypropylene, EPP, with a density of 50 kg/m^3.

At this point, the areas in which to measure deformation during the test, using DIC image analysis, were selected. We chose regions with easy optical access and as flat a distribution as possible, both to enable cameras to focus on a larger area and to ensure easier processing of the experimental data collected. The areas were chosen on different faces of the tested component, where significant and design-relevant deformations could be measured. Once identified and located, the areas were spray-painted and speckled to create a random pattern of black dots on a white background.

Before conducting the test, the protruding areas that allowed for assembly were removed from the part to simplify the geometry, also in view of the upcoming simulation. All the protrusions needed for the mounting and positioning of components were removed from both the base and the upper face, in order to ensure that there was a stable support on the bottom and a more uniform pressure distribution on the top face between the component and the loading plate.

4.2. Experimental Setup

The compression test was performed by placing the part to be tested on a base fixed to the lower crosshead of the tensile machine, as shown in Figure 4. The test was conducted in displacement control mode, applying a 10 mm downward displacement of the crosshead

at a speed of 1 mm/min. To distribute the pressure on the upper surface, we used an aluminum plate that conformed to the shape of the part.

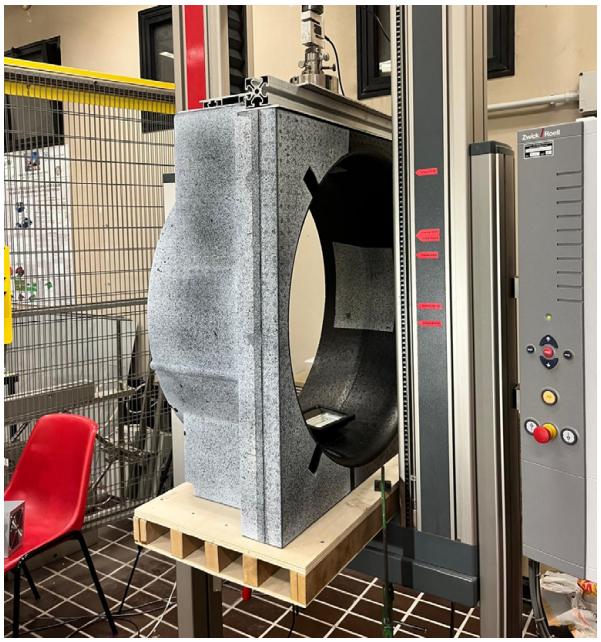
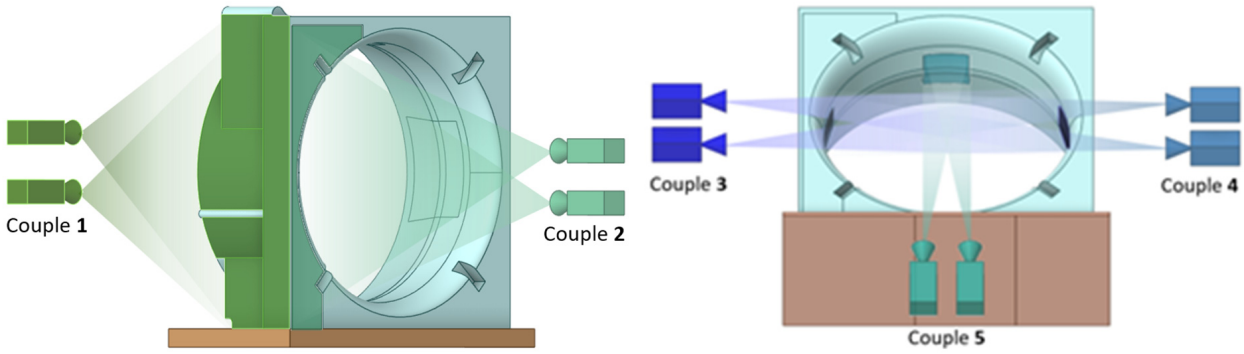


Figure 4. Compression test on the component.

The cameras were positioned to capture one of the side faces of the part, half of the back, as shown in Figure 5a, and three internal areas of the circular opening, as shown in Figure 5b.



(**a**) (**b**)

Figure 5. Setup: (**a**) positioning of cameras to grab the external speckled areas; (**b**) positioning of cameras to grab the internal speckled areas.

The measurement of deformations during the test was carried out using digital image correlation on five measurement areas [17,18]. Since these areas were located in distant regions and on perpendicular faces of the part, as shown in Figure 5, there was no overlapping in the fields of view of the cameras [19]. Therefore, to obtain a 3D measurement of the deformations, ten cameras were used, two for each monitored area. Each system, consisting of a couple of cameras, was calibrated separately. All data and calibration results of camera couples are reported in Table 2.

Table 2. Information and calibration results of camera couples.

	COUPLE 1	COUPLE 2	COUPLE 3	COUPLE 4	COUPLE 5
CMOS camera	FLIR BlackflyS BFS-U3	Pixelink®PL-B741F	Lucid PHX0 16S-MC	Lucid PHX0 16S-MC	Lucid PHX0 16S-MC
Lens	25 mm C-mount	16 mm C-mount	12 mm C-mount	12.5 mm C-mount	25 mm C-mount
Image resolution	4096 × 2160, 8 bit	1280 × 1024, 8 bit	1440 × 1080, 8 bit	1440 × 1080, 8 bit	1440 × 1080, 8 bit
Field of view	90 × 50 mm	80 × 65 mm	35 × 25 mm	35 × 25 mm	20 × 15 mm
Pixel to mm	1 pixel = 0.022 mm	1 pixel = 0.062 mm	1 pixel = 0.024 mm	1 pixel = 0.024 mm	1 pixel = 0.013 mm
Stereo-angle	19.69°	5.78°	12.76°	8.13°	7.53°
Pattern technique	Matt white spray paint base coat with black				
DIC technique	Stereo correlation				
DIC software	MatchID, version 2024.2.0				
Image filtering	Gaussian, 5 × 5 pixel kernel				
Subset size	45 pixels	11 pixels	35 pixels	27 pixels	35 pixels
Step size	10 pixels	3 pixels	10 pixels	10 pixels	10 pixels
Shape function	Affine				
Matching criterion	Zero-normalized sum of square differences				
Interpolant	Bi-cubic spline				
Stereo transform	Affine				

4.3. Processing of DIC Results

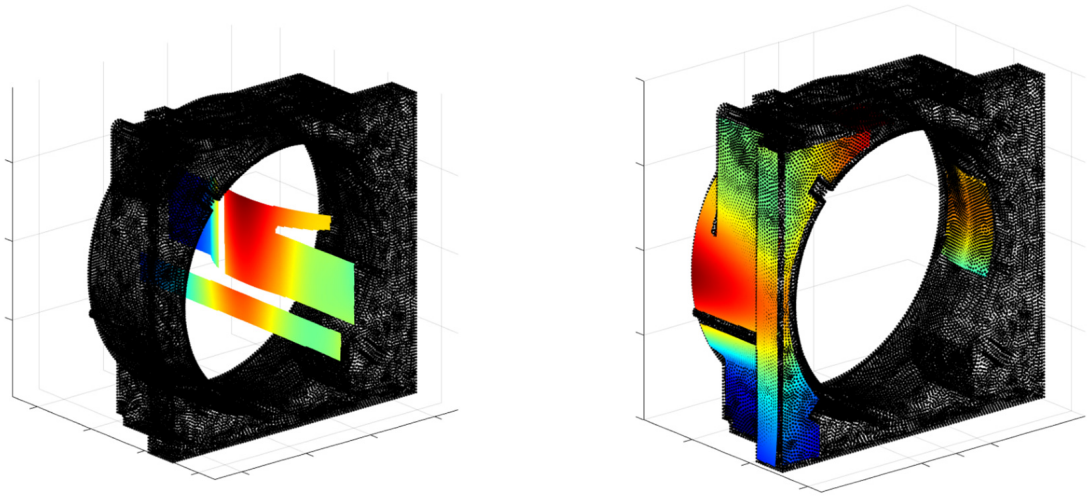
From the image processing performed with the MatchID software 2024 2.0, we obtained point clouds that represent the centers of the subsets. Associated with these points, we exported the displacement data measured during the test in the three directions (u, v, z). The coordinates of the points that define the measured areas were calculated relative to a fictitious reference system associated with each camera pair, defined in the software as "central camera". Obviously, since the central camera reference systems differ for each camera pair, the maps of the measured areas were not aligned with each other as in the actual shape. As we did not know the relative position of these five reference systems, we were unable to reconstruct the actual mutual position of the areas where the measurement was performed.

To achieve this, it was necessary to define a global reference system: for this purpose, the 3D CAD reference system was chosen. The part's geometry was represented, in a 3D graph, by plotting the position of the mesh nodes, generated in Ansys.

At this point, on the map of the measured area, a point, P', with local coordinates (X', Y', Z') was identified. The physical counterpart, P, of this point, in the real geometry, was known through geometric considerations. Point P has coordinates (X, Y, Z) relative to the chosen global reference system.

Based on this geometric relationship, it was possible to define a transformation matrix that allowed conversion from the local reference system into a global one.

By applying this method to all five point-clouds obtained from the deformation measurements, the results could be visualized within a global reference system, and even attached on the part's geometry, as shown in Figure 6.



(**a**) (**b**)

Figure 6. (**a**) Initial spatial orientation of displacement map; (**b**) displacement maps attached to CAD geometry, after applied transformation.

5. Results and Discussion

This section presents the corresponding numerical simulation conducted using Finite Element (FE) analysis after we performed the compression test. The aim was to compare the experimental results with the numerical data to assess their accuracy and consistency.

The numerical simulation allowed us to examine the behavior of the material under controlled conditions that closely replicate the experimental setup. Furthermore, it enabled us to identify potential discrepancies or correlations between the two methods. Such comparative analysis will not only validate the FE model's accuracy but also provide deeper insights into the material's mechanical properties and performance under compression.

In the following sections, we will delve into the specifics of FE analysis, detailing the parameters, boundary conditions, and material properties used in the simulation. The results will be critically compared with the experimental data to ensure consistency and precision in our findings.

5.1. Numerical Simulation

For the FE analysis, Ansys Workbench 2024 R2 software was used. A static structural analysis was conducted, and the material model used was the nonlinear third-order Ogden hyperfoam model, within which the parameters of the calibration, shown in Table 1, were inserted. To reproduce real operating conditions as faithfully as possible, two more pieces, in addition to the principal component, were simulated. The first one was the wood support piece, and the second one was the aluminum plate used for loading, as shown in Figure 4. Furthermore, we calibrated the stiffness of the support in order to be closer to real conditions.

Both types of contact were chosen to be frictional, and the friction coefficient was set to 0.2 between the component and the upper plate, while the friction coefficient was set to 0.5 between the component and the lower support [20].

All the components were meshed with the tetrahedral element. Following a mesh sensitivity analysis, we found that a 15 mm mesh size could fit the model well. Since the plates were not a major structure during the test, a 20 mm mesh size was selected for both lower and upper plates.

In the contact area where the support was placed on the machine's crosshead, the *fixed support* constraint was applied in Ansys, while a *vertical displacement* of 10 mm was

imposed on the loading plate. The results of the compression analysis will be compared to the results of the experimental test obtained through DIC.

5.2. Comparison of Results

The first comparison focuses on the force results, which are illustrated in Figure 7. This figure features two distinct curves: one representing the experimental force measured during the compression test and the other corresponding to the force developed during the FEM simulation. Upon examining the curves, it is evident that the deviation between the experimental and numerical results is minimal, indicating a high degree of correlation between the two methods.

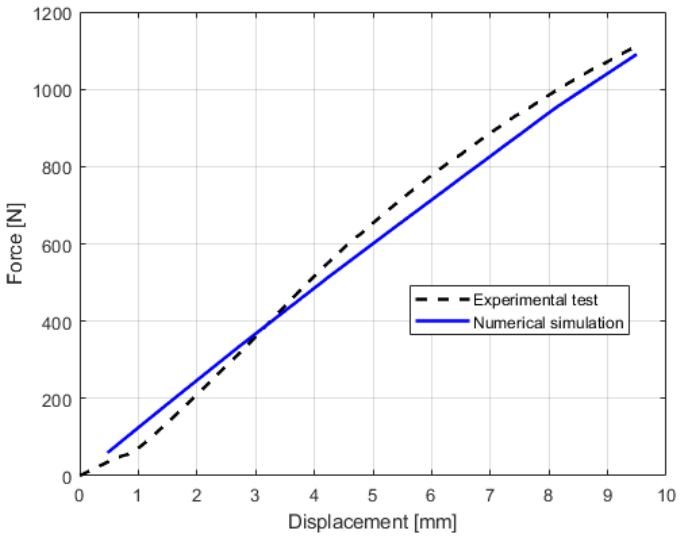
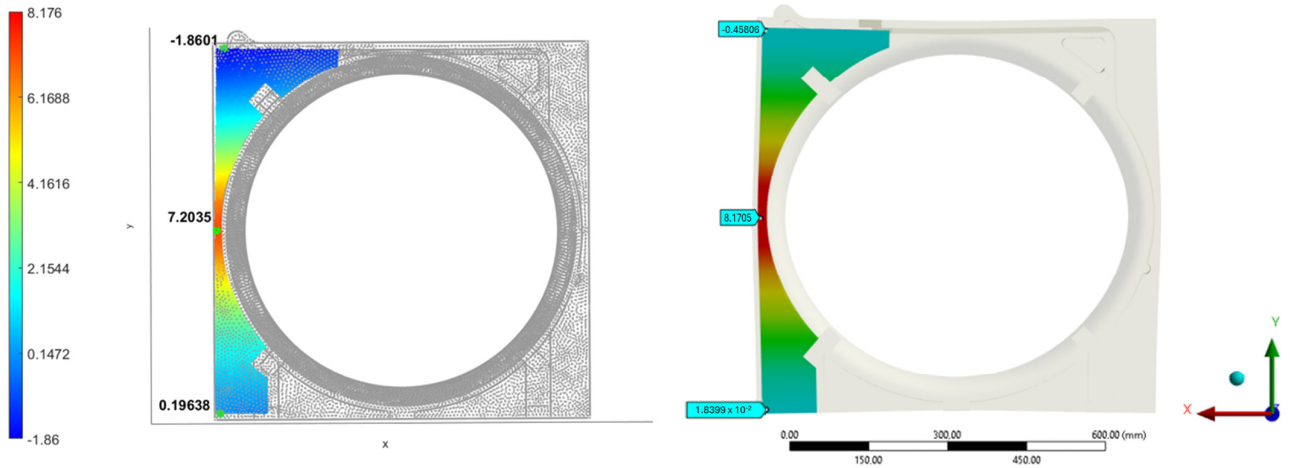


Figure 7. Comparison between experimental test force and numerical simulation force.

This close alignment suggests that the FEM simulation effectively captures the mechanical response of the material, validating the accuracy of the numerical model.

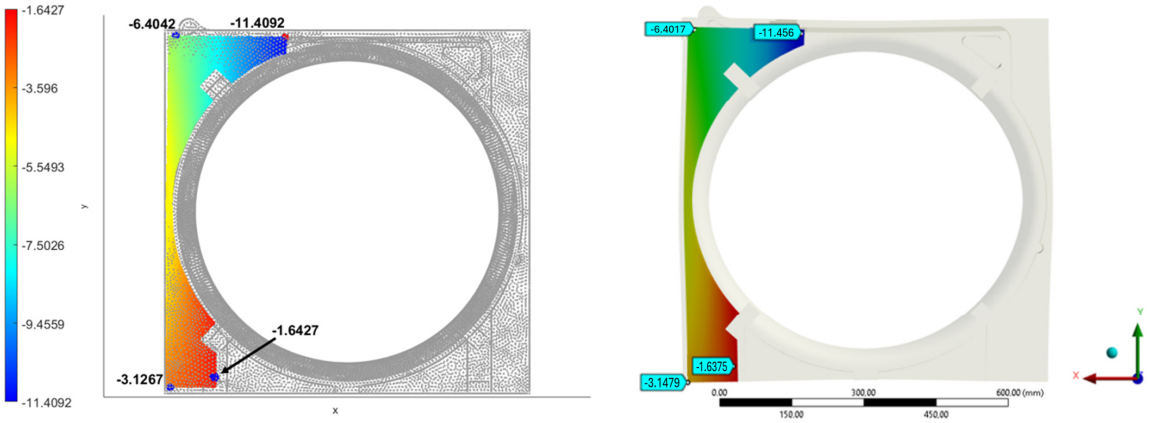
The experimental and numerical results were thoroughly analyzed and compared, with a particular emphasis on the most representative areas to ensure the accuracy of the most critical regions of the tested component.

Figures 8 and 9 compare the displacement results along the X axis and the Y axis, respectively, for the back zone, highlighting the correspondence between the experimental and simulated data in this key area.



(**a**) (**b**)

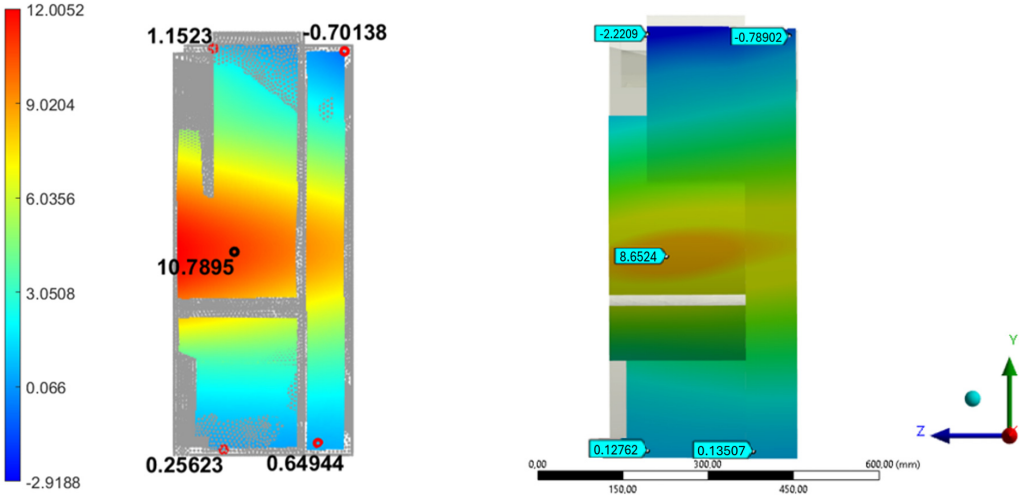
Figure 8. X displacement in frontal zone for (**a**) experimental test; (**b**) numerical simulation.



(**a**) (**b**)

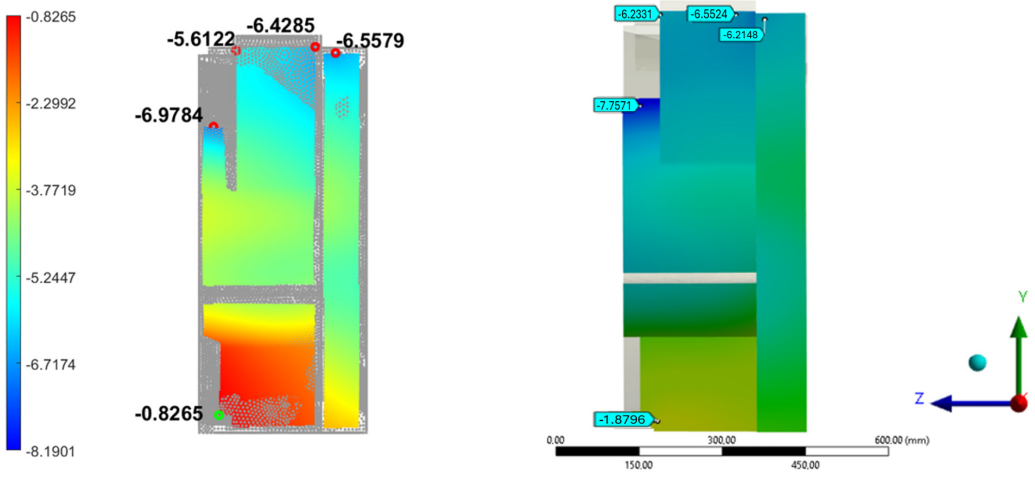
Figure 9. Y displacement in frontal zone for (**a**) experimental test; (**b**) numerical simulation.

Figures 10 and 11 provide a detailed comparison of the displacement results along the X axis and Y axis, respectively, for the lateral zone of the component.



(**a**) (**b**)

Figure 10. X displacement in lateral zone for (**a**) experimental test; (**b**) numerical simulation.



(**a**) (**b**)

Figure 11. Y displacement in lateral zone for (**a**) experimental test; (**b**) numerical simulation.

The results of the comparison, presented in Figures 8–11, show an excellent correlation between the experimental and numerical strain data. Any discrepancies observed are attributable to the difficulty in precisely replicating the boundary conditions applied during the test in the simulation.

6. Conclusions

In this paper, we present the calibration of a hyperelastic material model, Ogden foam, using experimental data obtained from uniaxial and simple shear tests. This model was employed in the simulation of a compression test performed on an industrial component made entirely of expanded polypropylene (EPP). Experimental strain measurements were obtained using Digital Image Correlation.

From the comparison between the results obtained through an optical analysis of the experimental test and those from the simulation, we can affirm that uniaxial and simple shear tests are sufficient to calibrate a hyperelastic model capable of describing the structural behavior of expanded polypropylene with reasonable accuracy even in complex deformation states.

Author Contributions: Conceptualization, C.S.; methodology, C.S. and G.C.; software, G.C.; validation, G.C.; formal analysis, V.I.; investigation, V.I.; resources, G.Z.; data curation, G.C. and V.I.; writing—original draft preparation, C.S.; writing—review and editing, M.S.; visualization, V.I. and G.Z.; supervision, M.S. All authors have read and agreed to the published version of the manuscript.

Funding: This research received no external funding.

Institutional Review Board Statement: Not applicable.

Informed Consent Statement: Not applicable.

Data Availability Statement: No publicly archived dataset is available for this work.

Conflicts of Interest: The authors declare no conflict of interest.

References

1. Mills, N. *Polymer Foam Handbook: Engineering and Biomechanics Applications and Design Guide*; Elsevier Science: Amsterdam, The Netherlands, 2007.
2. Begonia, M.; Rowson, B.; Scicli, B.; Goff, J. Laboratory evaluation of climbing helmets: Assessment of linear acceleration. *Smart Mater. Struct.* **2023**, *32*, 034003. [CrossRef]
3. Sasso, M.; Sarasini, F.; Mancini, E.; Lattanzi, A.; Tirillò, J.; Sergi, C. Experimental Characterization and Numerical Modelling of the Impact Behavior of PVC Foams. *Exp. Mech.* **2023**, *63*, 823–837. [CrossRef]
4. Zhao, J.; Wang, G.; Wang, C.; Park, C. Ultra-lightweight, super thermal isulation and strng PP/CNT microcellular foams. *Compos. Sci. Technol.* **2020**, *191*, 108084. [CrossRef]
5. Huang, Y.; Zhu, H.; Assima, D.; Wang, Z.; Li, M.; Zhao, X. Test and Analysis of the Sound Insulation Performance of Four Types of Timber Structure Floors under Jumping Excitation. *J. Renew. Mater.* **2021**, *9*, 829–840. [CrossRef]
6. Rahimidehgolan, F.; Altenhof, W. Compressive behavior and deformation mechanisms of rigid polymeric foam: A review. *Compos. Part B Eng.* **2023**, *253*, 110513. [CrossRef]
7. Ogden, R. *Non-Linear Elastic Deformation*; Dover Publications: Mineola, NY, USA, 1984.
8. Brown, R. *Handbook of Polymer Testing*; Rapra Technology Limited: Shropshire, UK, 2002.
9. International Digital Image Correlation Society. A Good Practices Guide for Digital Image Correlation. 2018. Available online: https://idics.org/guide/DICGoodPracticesGuide_PrintVersion-V5h-181024.pdf (accessed on 26 February 2025).
10. Miyauchi, K. On a simple shear deformation. *Sci. Pap. Inst. Phys. Chem. Res.* **1987**, *81*, 57–67.
11. Bouvier, S.; Haddadi, H.; Levée, P.; Teodosiu, C. Simple shear tests: Experimental techniques and characterization of the plastic anisotropy of rolled sheets at large strains. *J. Mech. Work. Technol.* **2006**, *172*, 96–103. [CrossRef]
12. Bower, A. *Applied Mechanics of Solids*; CRC Press: Boca Raton, FL, USA, 2010.
13. Moreira, D.; Nunes, L. Comparison of simple and pure shear for an incompressible isotropic hyperelastic material under large deformation. *Polym. Test.* **2013**, *32*, 240–248. [CrossRef]
14. Ogden, R.; Saccomandi, G.; Sgura, I. Fitting hyperelastic models to experimental data. *Comput. Mech.* **2004**, *34*, 484–502. [CrossRef]

15. Lee, J.; Hwang, E.; Kacker, R. True value, error and measurement uncertainty. *Accredit. Qual. Assur.* **2022**, *27*, 235–242. [CrossRef]
16. Petre, M.; Erdemir, A.; Cavanangh, P. Determination of elastomeric foam parameters for simulations of complex loading. *Comput. Methods Biomech. Biomed. Eng.* **2006**, *9*, 231–242. [CrossRef] [PubMed]
17. Morrichelli, L.; Chiappini, G.; Lattanzi, E. Santecchia and M. Rossi. Combined effect of process variables on the plastic behaviour of 316L stainless steel printed by L-PBF. *Strain* **2023**, *59*, e12438. [CrossRef]
18. Simoncini, M.; Forcellese, A.; Mancini, E.; Chiappini, G.; Sasso, M. Experimental and numerical investigation no forming limit curves of AA6082 aluminium alloy at high strain rates. *Int. J. Adv. Manuf. Technol.* **2021**, *112*, 1973–1991. [CrossRef]
19. Melesa, M.; Malowany, K.; Zagorski, A. Non-destructive testing of industrial structures with the use of multi-camera Digital Image Correlation method. *Eng. Fail. Anal.* **2016**, *69*, 122–134. [CrossRef]
20. Kikuchi, K.; Iasawa, A.; Omori, M.; Mayama, H.; Nonomura, Y. Friction Dynamics of Foams under Nonlinear Motion. *ACS Omega* **2022**, *7*, 16515–16523. [CrossRef] [PubMed]

Disclaimer/Publisher's Note: The statements, opinions and data contained in all publications are solely those of the individual author(s) and contributor(s) and not of MDPI and/or the editor(s). MDPI and/or the editor(s) disclaim responsibility for any injury to people or property resulting from any ideas, methods, instructions or products referred to in the content.